


 Cite this: *RSC Adv.*, 2019, **9**, 11912

## Mesoporous MnO<sub>x</sub>–CeO<sub>2</sub> composites for NH<sub>3</sub>-SCR: the effect of preparation methods and a third dopant†

 Li Weiman, <sup>abcd</sup> Liu Haidi<sup>a</sup> and Chen Yunfa <sup>\*ad</sup>

In this study, different preparation methods including an oxalate route, a nano-casting strategy and a traditional co-precipitation route were applied to obtain MnO<sub>x</sub>–CeO<sub>2</sub> mixed oxides for selective catalytic reduction (SCR) of NO with NH<sub>3</sub>. The catalyst prepared from the oxalate route showed improved performance for NO<sub>x</sub> conversion and SO<sub>2</sub> + H<sub>2</sub>O durability. To further improve the SO<sub>2</sub> and H<sub>2</sub>O resistance of catalysts, ternary oxides were prepared from the oxalate route. The catalysts were studied by X-ray diffraction (XRD), Brunauer–Emmett–Teller (BET) surface area analysis, X-ray photoelectron spectroscopy (XPS), H<sub>2</sub> temperature-programmed reduction (H<sub>2</sub>-TPR), NH<sub>3</sub> temperature-programmed desorption (NH<sub>3</sub>-TPD), SO<sub>2</sub> temperature-programmed desorption (SO<sub>2</sub>-TPD), and *in situ* diffuse reflectance infrared fourier transform spectroscopy (*in situ* DRIFTS). The nickel–manganese–cerium ternary oxide showed the best SO<sub>2</sub> and H<sub>2</sub>O durability. The reason can be ascribed to its smaller pores, amorphous structure, and moderate amount of surface Mn<sup>3+</sup>/oxygen species, which could decrease chemical adsorption of SO<sub>2</sub>.

Received 28th January 2019  
 Accepted 29th March 2019

DOI: 10.1039/c9ra00731h  
[rsc.li/rsc-advances](http://rsc.li/rsc-advances)

## 1 Introduction

Nitrogen oxides (NO<sub>x</sub>), emitted from combustion of fossil fuels in industrial stationary sources, have caused a series of environmental problems such as acid rain, haze, and ozone depletion. Selective catalytic reduction of NO<sub>x</sub> by ammonia (NH<sub>3</sub>-SCR) is one of the most promising NO<sub>x</sub> abatement technologies. The widely used catalyst in NH<sub>3</sub>-SCR is V<sub>2</sub>O<sub>5</sub>–WO<sub>3</sub>(MoO<sub>3</sub>)/TiO<sub>2</sub>, whose optimum working temperature is higher than 350 °C. In practical application, the SCR reactor is usually located downstream of dust and SO<sub>2</sub> removing modules to avoid catalyst deactivation from dust, SO<sub>2</sub> and other poisoners. As a result, the temperature of flue gas is usually lower than 300 °C, and the flue gas has to be reheated to meet the V–W–Ti working temperature, which will increase the cost of deNO<sub>x</sub>. Therefore, a better choice is to develop catalysts with high deNO<sub>x</sub> efficiency, high resistance to water vapor/SO<sub>2</sub>, and a low working temperature window.

Ce–Mn composites have been reported widely for their excellent low temperature deNO<sub>x</sub> efficiency and high N<sub>2</sub> selectivity. The catalytic ability of Ce–Mn composites is related to the pore structure, specific area, and redox behavior.<sup>1–3</sup> For example, MnO<sub>x</sub>–CeO<sub>2</sub> nanosphere catalyst showed superior performance compared to its counterpart MnO<sub>x</sub>–CeO<sub>2</sub> without any defined structural morphology.<sup>4</sup> MnO<sub>x</sub>–CeO<sub>2</sub> hollow nanotube synthesized through the interfacial oxidation–reduction reaction showed 96% NO<sub>x</sub> conversion at 100 °C, and the authors attributed to the uniform distribution of active species and the hollow porous architectures which provided huge specific surface area and sufficient acidic sites.<sup>5</sup> However, the activity of MnO<sub>x</sub>–CeO<sub>2</sub> composites is still low in the presence of SO<sub>2</sub> and H<sub>2</sub>O. Lots of efforts have been done to improve SO<sub>2</sub> and H<sub>2</sub>O resistance of MnO<sub>x</sub>–CeO<sub>2</sub> composites. For example, adding a third dopant (Sn, Cr, W, Eu *etc.*) into MnO<sub>x</sub>–CeO<sub>2</sub> composites can further improve the deNO<sub>x</sub> efficiency and SO<sub>2</sub> resistance.<sup>6–9</sup> Cobalt or nickel doped MnO<sub>x</sub>–CeO<sub>2</sub> catalysts showed high SCR activity and good tolerance of SO<sub>2</sub>, and the authors suggested different SCR reaction pathways and mechanisms of SO<sub>2</sub> tolerance between Co/Ni doped and un-doped MnO<sub>x</sub>–CeO<sub>2</sub>.<sup>10</sup> Mesoporous catalysts have been proved a good choice to improve SO<sub>2</sub> resistance.<sup>11</sup> Zha prepared a MnCeW catalyst on mesoporous TiO<sub>2</sub> spheres, and the catalyst showed excellent SCR activity in a wide temperature range.<sup>9</sup> Fe<sub>2</sub>O<sub>3</sub> promoted halloysite-supported CeO<sub>2</sub>–WO<sub>3</sub> catalysts showed improved NO<sub>x</sub> reduction in the presence of SO<sub>2</sub>, and the authors confirmed that the increase of Brønsted acid site derived from Fe<sub>2</sub>O<sub>3</sub> promotion is the main cause.<sup>12</sup>

<sup>a</sup>State Key Laboratory of Multi-phase Complex Systems, Institute of Process Engineering, Chinese Academy of Sciences, Beijing 100190, China. E-mail: chenyf@ipe.ac.cn

<sup>b</sup>University of Chinese Academy of Sciences, No. 19A Yuquan Road, Beijing 100049, China

<sup>c</sup>Zhongke Langfang Institute of Process Engineering, Langfang Economic & Technical Development Zone, Fenghua Road No. 1, Hebei Province, China

<sup>d</sup>CAS Center for Excellence in Urban Atmospheric Environment, Xiamen 361021, China

† Electronic supplementary information (ESI) available. See DOI: 10.1039/c9ra00731h



Based on previous studies, the catalytic performance of NH<sub>3</sub>-SCR activity, including NO<sub>x</sub> conversion efficiency, N<sub>2</sub> selectivity and H<sub>2</sub>O + SO<sub>2</sub> resistance are mainly determined by following factors: pore structure and surface area, the distribution of manganese and cerium states, and the active oxygen species including adsorbed oxygen, oxygen vacancy and lattice oxygen, as well as surface acidity. Inspired by the above studies, we have fabricated MnO<sub>x</sub>-CeO<sub>2</sub> with different pore structures by various methods, and the relationship of NH<sub>3</sub>-SCR ability and structure was discussed. To further improve the H<sub>2</sub>O + SO<sub>2</sub> resistance of the catalysts, nickel/cobalt was introduced to the MnO<sub>x</sub>-CeO<sub>2</sub> catalysts, and the catalytic performance was evaluated.

## 2 Experimental section

### 2.1 Catalysts preparation

All chemical reagents used in this work including Mn(ac)<sub>2</sub>·4H<sub>2</sub>O (99.0%), Ce(ac)<sub>3</sub>·0.5H<sub>2</sub>O (99.0%), Co(ac)<sub>2</sub>·4H<sub>2</sub>O (99.0%), Ni(ac)<sub>2</sub>·4H<sub>2</sub>O (99.0%), C<sub>2</sub>H<sub>2</sub>O<sub>4</sub>·2H<sub>2</sub>O (99.5%), Mn(NO<sub>3</sub>)<sub>2</sub> (50% wt), Ce(NO<sub>3</sub>)<sub>3</sub>·6H<sub>2</sub>O, Co(NO<sub>3</sub>)<sub>2</sub>·6H<sub>2</sub>O, Ni(NO<sub>3</sub>)<sub>2</sub>·6H<sub>2</sub>O and NaOH were purchased from Xilong Cop. (China) and used without further purification. To prepare MnO<sub>x</sub>-CeO<sub>2</sub> composites with different pore structures, an oxalate route, a nano-casting strategy and a simple precipitation method were applied.

In an oxalate route, calculated metal salts (the molar ratio of Mn and Ce was 6 : 4) were dissolved in deionized water at room temperature, labeled as solution A. Then, C<sub>2</sub>H<sub>2</sub>O<sub>4</sub>·2H<sub>2</sub>O (the molar ratio of C<sub>2</sub>H<sub>2</sub>O<sub>4</sub>·2H<sub>2</sub>O to total metals is 1.2) was dissolved in ethanol, labeled as solution B. The mixtures of A and B were stirred for 24 h. The precipitates were washed, dried, and finally calcined at 550 °C for 4 h. The sample was labeled as 6Mn4Ce-O. Nickel or cobalt doped MnO<sub>x</sub>-CeO<sub>2</sub> composite was prepared as the same procedure. The samples were denoted as 1Ni6Mn3Ce-O and 1Co6Mn3Ce-O, respectively.

In a nano-casting route, KIT-6 silica was employed as a hard template, and the MnO<sub>x</sub>-CeO<sub>2</sub> catalyst was synthesized by a simple “two-solvent” approach. KIT-6 silica was prepared as previously reported studies.<sup>13</sup> In a typical procedure, 1.0 g KIT-6 was suspended in 80 ml *n*-hexane and stirred at room temperature for 2 h. Then a mixed solution of Mn(NO<sub>3</sub>)<sub>2</sub> and Ce(NO<sub>3</sub>)<sub>3</sub> was added slowly with vigorous stirring. After stirred overnight, the mixture was filtered and dried at 80 °C for 24 h. The obtained powder was calcined at 550 °C for 4 h, with a heating rate of 2 °C min<sup>-1</sup> in air. Finally, the sample was treated three times with a 2 M NaOH solution, washed to pH ~ 7 and dried at 80 °C. The product was denoted as 6Mn4Ce-N.

As a comparison, the third MnO<sub>x</sub>-CeO<sub>2</sub> sample was synthesized by a co-precipitation method using NH<sub>3</sub> H<sub>2</sub>O as precipitant, and the sample was labeled as 6Mn4Ce-C.

### 2.2 Catalytic activity tests

Before SCR activity test, the catalysts were crushed and sieved to 40–60 mesh. A fixed-bed quartz flow reactor was used to perform SCR activity test. The typical reactant gas contained 200 ppm NO<sub>x</sub>, 200 ppm NH<sub>3</sub>, 5% O<sub>2</sub>, 100 ppm SO<sub>2</sub> (when used), 5 vol% H<sub>2</sub>O (when used) and balance of N<sub>2</sub>. In a typical experiment,

100 mg catalyst was used, corresponding to gas volume hourly space velocity (GHSV) of 72 000 h<sup>-1</sup>. The temperature range was set to 100–300 °C. An FTIR spectrometer (Bruker Vertex 70 spectrometer, USA) equipped with a heated, multiple path gas cell (10 m) was used to collect the FTIR spectra. The NO<sub>x</sub> conversion and N<sub>2</sub> selectivity were calculated as follows:

$$\text{NO}_x \text{ conversion}(\%) = \frac{[\text{NO}]_{\text{in}} - [\text{NO}]_{\text{out}}}{[\text{NO}]_{\text{in}}} \times 100\%,$$

$$\text{N}_2 \text{ selectivity}(\%)$$

$$= \frac{[\text{NO}]_{\text{in}} + [\text{NH}_3]_{\text{in}} - [\text{NO}_2]_{\text{out}} - 2[\text{N}_2\text{O}]_{\text{out}}}{[\text{NO}]_{\text{in}} + [\text{NH}_3]_{\text{in}}} \times 100\%$$

### 2.3 Characterization

XRD patterns were recorded on a PANalytical X'Per PRO X-ray diffraction using Ni filtered Cu K $\alpha$  ( $\lambda = 0.15418$  nm) radiation at 40 kV and 30 mA, in  $2\theta$  from 5° to 90° with a scanning step of 0.0334°. The specific surface area and pore size distributions of all catalysts were obtained according to the Brunauer–Emmett–Teller (BET) and Barrett–Joyner–Halenda (BJH) methods, respectively, using N<sub>2</sub> adsorption–desorption method on an automatic surface analyzer (SSA-7300, BJ-Builder, China) at 77 K. Each sample was pre-degassed at 150 °C for 3 h. Surface species of as-prepared catalysts were determined by X-ray photoelectron spectroscopy (XPS) using a XLESCALAB 250 Xi electron spectrometer (Thermo Scientific, USA) with monochromatic Al K $\alpha$  radiation (1486.6 eV).

H<sub>2</sub> temperature-programmed reduction (H<sub>2</sub>-TPR) was conducted on a Micromeritics Chemisorb 2720 analyzer (Micromeritics, USA) at a heating rate of 10 °C min<sup>-1</sup> with 5% H<sub>2</sub>/Ar gas. The H<sub>2</sub> consumption was recorded continuously to investigate reduction abilities. NH<sub>3</sub> temperature-programmed desorption (NH<sub>3</sub>-TPD) was performed on a Micromeritics Autochem II 2920 analyzer (Micromeritics, USA). The catalysts were firstly heated to 300 °C for 1 h in helium, and then cooled down to 50 °C. After saturated in pure NH<sub>3</sub> for 30 min, the samples were purged in pure helium for 1 h to remove the physically adsorbed NH<sub>3</sub>. The TPD curve was finally recorded in helium from 50 °C to 600 °C at a heating rate of 10 °C min<sup>-1</sup>. SO<sub>2</sub> temperature-programmed desorption (SO<sub>2</sub>-TPD) was performed on a TP5080B apparatus (Tianjin XQ, China). 50 mg of 40–60 mesh catalysts was firstly heated to 300 °C for 1 h in 30 ml min<sup>-1</sup> helium, and then cooled to 200 °C. The catalysts were saturated in 2000 ppm SO<sub>2</sub> for 1 h, and then purged with 30 ml min<sup>-1</sup> helium for 1 h to remove residue SO<sub>2</sub> at 200 °C. At last, the catalyst was heated from 200 °C to 850 °C in helium at 10 °C min<sup>-1</sup>.

A Bruker Vertex 70 spectrometer (Bruker, USA) equipped with diffuse reflectance accessory (PIKE, and MCT/A detector cooled by liquid nitrogen) was used for recording the *in situ* DRIFT spectra of the samples. Twenty mg KBr powder was placed under proper amount of samples, and a specially made steel stick was used to smash the sample to a flat surface. The



sample was pretreated at 300 °C for 2 h in N<sub>2</sub> (50 ml min<sup>-1</sup>). The reaction system was cooled to 200 °C in N<sub>2</sub>, and the spectra were collected as background. The spectra were recorded by accumulating 32 scans at a resolution of 4 cm<sup>-1</sup>.

### 3 Results and discussion

#### 3.1 NH<sub>3</sub>-SCR performance

All composites prepared by different methods were tested for NH<sub>3</sub>-SCR in temperature range of 100–350 °C, as shown in Fig. 1A. The NO<sub>x</sub> conversion of all catalysts first increased and then decreased. The NO<sub>x</sub> conversion rates at the whole temperature range of the three catalysts followed the sequence of 6Mn4Ce-O > 6Mn4Ce-C > 6Mn4Ce-N. The NO<sub>x</sub> conversion of 6Mn4Ce-O reached its maximum of 99% at ~170 °C; and its NO<sub>x</sub> conversion rate remained >80% at the temperature range of 120–275 °C. The NO<sub>x</sub> conversion of 6Mn4Ce-C was slightly lower than that of 6Mn4Ce-O. The catalyst prepared from nanocasting route showed the worst catalytic performance. Resistance to H<sub>2</sub>O and SO<sub>2</sub> is an important factor that to be concerned in the evaluation of NH<sub>3</sub>-SCR catalysts, as there is more or less SO<sub>2</sub> and H<sub>2</sub>O in gas that to be managed. The H<sub>2</sub>O + SO<sub>2</sub> resistance of three samples is shown in Fig. 1B. After H<sub>2</sub>O + SO<sub>2</sub> was introduced into flue gas, the NO<sub>x</sub> conversion rate of

6Mn4Ce-O, 6Mn4Ce-N and 6Mn4Ce-C decreased to ~70%, ~62.5% and ~59%, respectively. This indicated that different structure of catalysts had a profound effect on resistance of H<sub>2</sub>O and SO<sub>2</sub>.

Addition of transition metal oxides (CrO<sub>x</sub>,<sup>14</sup> NiO,<sup>10,15–17</sup> Co<sub>3</sub>O<sub>4</sub>,<sup>10</sup> SnO<sub>2</sub>,<sup>18,19</sup> *et al.*) into MnO<sub>x</sub> or CeO<sub>2</sub> were shown to improve the SCR activity in presence of SO<sub>2</sub> and H<sub>2</sub>O, by increasing the surface acidity concentration of Lewis or Brønsted acid sites.<sup>16,18,20</sup> Based on above results, the H<sub>2</sub>O and SO<sub>2</sub> resistance of sample prepared from oxalate route was better than other two samples. Therefore, we prepared Co/Ni doped MnO<sub>x</sub>–CeO<sub>2</sub> composites by oxalate route to further improve their resistance to H<sub>2</sub>O and SO<sub>2</sub>. As shown in Fig. 1C, addition of nickel or cobalt can both increase the NO<sub>x</sub> conversion rate at temperature range of 100–280 °C. For example, the NO<sub>x</sub> conversion of 1Ni6Mn3Ce-O and 1Co6Mn3Ce-O were 99% at 200 °C, slightly higher than that of 6Mn4Ce-O (~96% at 200 °C). Besides, the N<sub>2</sub> selectivity of 6Mn4Ce-O was lower than those of 1Ni6Mn3Ce-O and 1Co6Mn3Ce-O (Fig. 1C). The above results showed that addition of nickel or cobalt slightly improves the SCR activity and N<sub>2</sub> selectivity. The H<sub>2</sub>O and SO<sub>2</sub> resistance of transition metal oxide doped composites were shown in Fig. 1D. With co-existence of H<sub>2</sub>O and SO<sub>2</sub>, NO<sub>x</sub> conversion decreased sharply to 70%, 80% and 20% over 6Mn4Ce-O, 1Ni6Mn3Ce-O

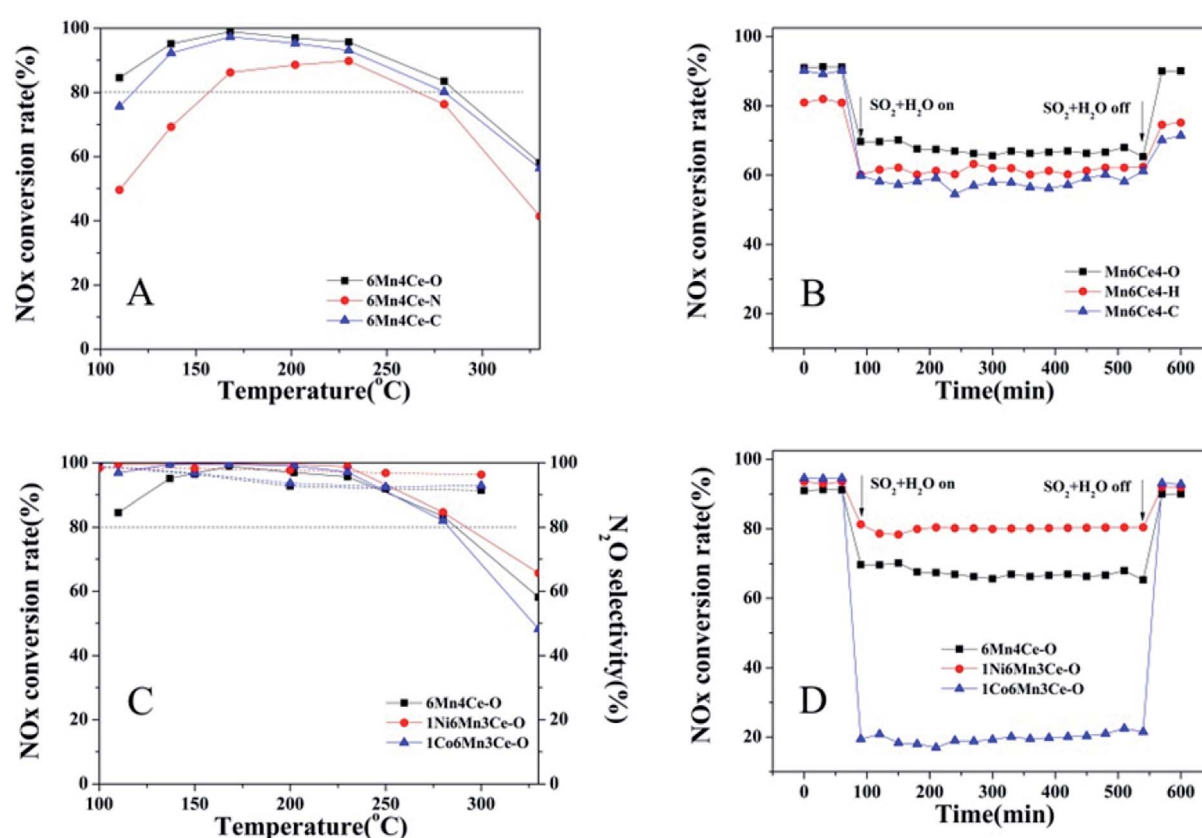


Fig. 1 (A) NO<sub>x</sub> conversion as a function of temperature over MnO<sub>x</sub>–CeO<sub>2</sub> prepared by different methods; (B) H<sub>2</sub>O + SO<sub>2</sub> resistance over MnO<sub>x</sub>–CeO<sub>2</sub> prepared by different methods at 200 °C; (C) NO<sub>x</sub> conversion as a function of temperature over nickel/cobalt doped MnO<sub>x</sub>–CeO<sub>2</sub>; (D) H<sub>2</sub>O + SO<sub>2</sub> resistance over nickel/cobalt doped samples by oxalate method at 200 °C; (reaction conditions: [NO<sub>x</sub>] = [NH<sub>3</sub>] = 200 ppm, [O<sub>2</sub>] = 5 vol%, [SO<sub>2</sub>] = 100 ppm, [H<sub>2</sub>O] = 5 vol% (when used), N<sub>2</sub> as balance gas, flow rate = 100 ml min<sup>-1</sup>, GHSV = 60 000 h<sup>-1</sup>).



and  $1\text{Co6Mn3Ce-O}$ , respectively. When  $\text{H}_2\text{O}$  and  $\text{SO}_2$  were cutoff, the deNO<sub>x</sub> activity of  $6\text{Mn4Ce-O}$ ,  $1\text{Ni6Mn3Ce-O}$  and  $1\text{Co6Mn3Ce-O}$  resumed. In previous studies,  $\text{MnO}_x\text{-CeO}_2$  composite exhibited low  $\text{SO}_2$  tolerance because of sulfate species formation. Therefore, many efforts have been done to improve the  $\text{SO}_2$  resistance of  $\text{MnO}_x\text{-CeO}_2$  catalysts. For example, novel  $\text{MnO}_x\text{-CeO}_2$  nano-sphere catalyst showed improved  $\text{SO}_2$  tolerance than  $\text{MnO}_x\text{-CeO}_2$  catalyst without defined structural morphology.<sup>4</sup>  $\text{CeO}_2\text{-MnO}_x$  showed relatively good resistance to  $\text{SO}_2$  because of its core-shell structure.<sup>21</sup> In our study, both preparation methods and addition of a third dopant were help to improve the resistance to  $\text{SO}_2$  and  $\text{H}_2\text{O}$ . This phenomenon illustrated structure, as well as different interaction among third dopants and Mn-Ce composites may play important roles in  $\text{NH}_3\text{-SCR}$ , which will further be discussed in following parts.

### 3.2 Structural properties

**3.2.1 XRD and BET analysis.** The XRD patterns of all samples were shown in Fig. 2. The diffraction peaks of  $6\text{Mn4Ce-O}$  mainly represented  $\text{CeO}_2$  (JCPDF#34-0394) and  $\text{Mn}_2\text{O}_3$  (JCPDF#41-1442). While the diffraction peaks of  $6\text{Mn4Ce-N}$  and  $6\text{Mn4Ce-C}$  exhibited broad reflections of  $\text{CeO}_2$ , no obvious peaks related to  $\text{MnO}_x$ .

The diffraction peaks of  $1\text{Ni6Mn3Ce-O}$  and  $1\text{Co6Mn3Ce-O}$  exhibited broad reflections of  $\text{CeO}_2$ , no obvious peaks related to  $\text{MnO}_x$ ,  $\text{NiO}$  or cobalt oxides. Similar results<sup>22</sup> were reported in the case of  $\text{Ni}(0.4)\text{-MnO}_x$  spinel. It is commonly accepted than amorphous structure is easy to embed and intercalate protons rapidly,<sup>23</sup> therefore promoting adsorption/desorption and redox reaction on the surface of catalysts.<sup>23,24</sup> In our study, although the deNO<sub>x</sub> efficiency and  $\text{N}_2$  selectivity of catalysts were similar, the  $\text{SO}_2 + \text{H}_2\text{O}$  resistance varied a lot. It can be concluded that amorphous structure caused by addition of a third dopant may be responsible for the good performance of catalysts.

The  $\text{N}_2$ -adsorption-desorption isotherms and corresponding Barrett-Joyner-Halenda (BJH) pore size distribution curves for

catalysts were shown in Fig. 3 (inset). The isotherms of all catalysts showed a characteristic type IV pattern, with a hysteresis loop of type H<sub>2</sub> in the IUPAC classification, indicating the existence of meso-pores and micro-pores. At low  $P/P_0$ , the isotherm curve of  $6\text{Mn4Ce-O}$  had a relatively lower slope than those of other catalysts, indicating its higher degree of crystallinity, consistent with XRD results. As shown in Fig. 3 (A, inset) and Table 1, the specific surface area of  $6\text{Mn4Ce-N}$  ( $152.116 \text{ m}^2 \text{ g}^{-1}$ ) was higher than  $6\text{Mn4Ce-O}$  ( $116.678 \text{ m}^2 \text{ g}^{-1}$ ) and  $6\text{Mn4Ce-C}$  ( $77.269 \text{ m}^2 \text{ g}^{-1}$ ); while the pore diameter followed the sequence of  $6\text{Mn4Ce-N} < 6\text{Mn4Ce-O} < 6\text{Mn4Ce-C}$ . This result showed that the specific surface area is not positively correlated with the NO<sub>x</sub> conversion, similar to the report from Qi.<sup>25</sup> Mesoporous materials present lots of edges and corners for adsorption of reactants; and the pores facilitate mass transfer at the gas-solid phase boundary.<sup>26</sup> Large surface area contributed more active sites, which would facilitate the adsorption of reactants. However, the  $\text{SO}_2$  and  $\text{H}_2\text{O}$  in flue gas may also occupy the active sites of catalysts, leading to a drop of SCR conversion. The smaller pores in catalysts from oxalate routes may possibly inhibit the reaction of NO<sub>x</sub>,  $\text{NH}_3$  with  $\text{SO}_2$  and  $\text{H}_2\text{O}$ . Although  $6\text{Mn4Ce-O}$  has a higher degree of crystallinity, which may not facilitate the synergistic effect between elements, the smaller pores in it can balance its structure.

For catalysts from a same oxalate route, a third dopant did not change the specific surface area significantly as shown in Table 1. However, the pore diameter of  $6\text{Mn4Ce-O}$  and  $1\text{Co6Mn3Ce-O}$  were among 1.5–2.5 nm. While for  $1\text{Ni6Mn3Ce-O}$ , the pore size distribution was among 1.5–2 nm and 2.5–10 nm, similar to previous study.<sup>27</sup> This indicated addition of nickel into  $\text{MnO}_x\text{-CeO}_2$  could change its pore structure, leading to a combination of macropores and mesopores. According to literature,<sup>28</sup> the release of gaseous  $\text{H}_2\text{O}$  and  $\text{CO}_x$  will create pores during the decomposition of oxalate chains chelated in corresponding precursors. In our study, nickel may regulate gas release during the thermo-decomposition precursors.

**3.2.2 Surface composition analysis.** The XPS results were shown in Fig. 4, and all spectra were calibrated with C1s (284.8

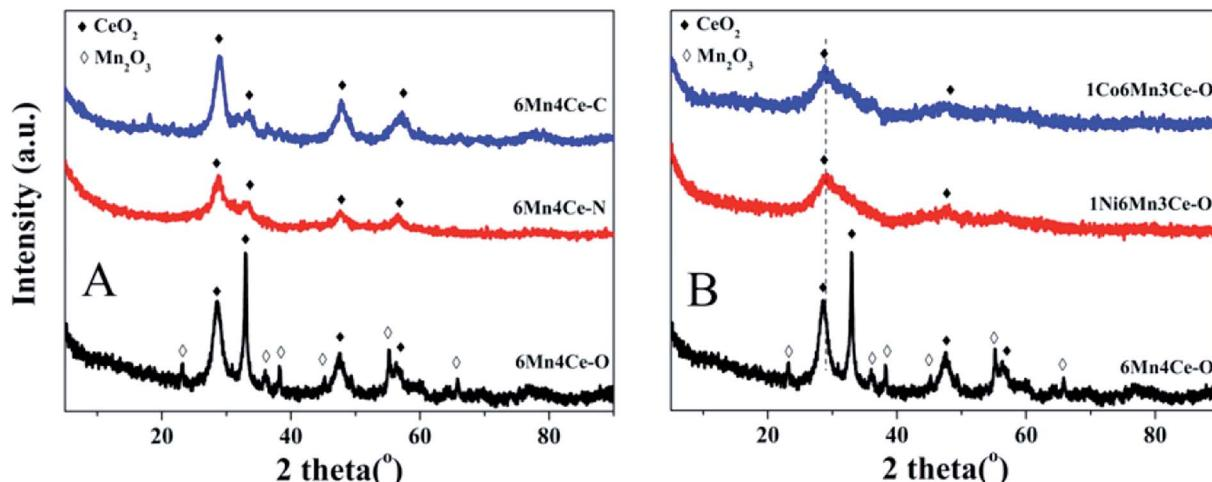


Fig. 2 XRD patterns of as-prepared samples, (A) samples from different methods, and (B) nickel or cobalt doped samples from oxalate route.



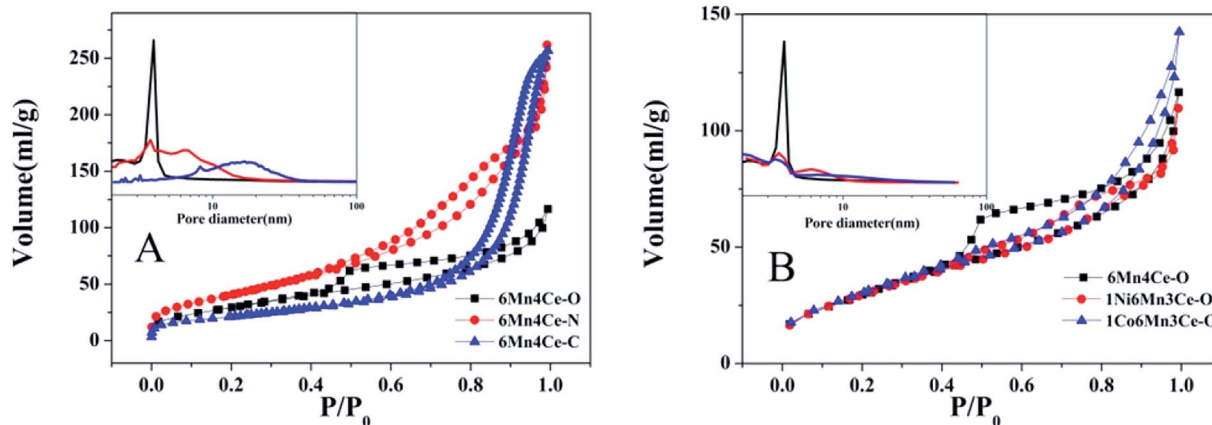


Fig. 3  $N_2$  adsorption/desorption isotherms and pore size distribution (inset) for samples (A) samples from different methods, and (B) nickel or cobalt doped samples from oxalate route.

Table 1 The structural data for all catalysts

	BET ( $m^2 g^{-1}$ )	Pore volume ( $ml g^{-1}$ )	Average pore diameter (nm)
6Mn4Ce-O	116.678	0.1686	6.5
6Mn4Ce-N	152.116	0.3955	10.7
6Mn4Ce-C	77.269	0.4036	20.6
1Ni5Mn4Ce-O	113.258	0.1428	6.0
1Co5Mn4Ce-O	116.926	0.1937	7.5

eV) before analysis. O1s spectra were fitted into two peaks. The peak centered at  $\sim 529.2$ – $529.7$  eV was related to surface lattice oxygen (denoted as  $O_{latt}$ ), and the peak at higher binding energy ( $\sim 532.4$  eV) was ascribed to surface chemisorbed oxygen (including adsorbed oxygen, hydroxyl and carbonate, denoted as  $O_{ads}$ ). Compared with 6Mn4Ce-O and 6Mn4Ce-N, the  $O_{latt}$  peak of 6Mn4Ce-C shifted to lower binding energy (529.7 eV to 529.2 eV). This phenomenon indicated that different synthesis method can regulate element valence. The relative ratios of  $O_{ads}/O_{latt}$  were 1.96, 1.26 and 1.09 for 6Mn4Ce-O, 6Mn4Ce-N and 6Mn4Ce-C, respectively.  $O_{ads}$  are considered as the active sites for SCR, because they can provide acid sites to adsorb  $NH_3$  to form  $NH_4^+$  or  $NH_3(ads)$ .<sup>29</sup> From this point of view, more  $O_{ads}$  species lead to improved activity and good  $H_2O$  and  $SO_2$  durability. The  $H_2O$  and  $SO_2$  durability sequence of 1Ni5Mn3Ce-O, 6Mn4Ce-O, and 1Co6Mn3Ce-O was consistent with  $O_{ads}/O_{latt}$  ratio (1Ni5Mn3Ce-O > 6Mn4Ce-O > 1Co6Mn3Ce-O). Again, this indicated oxalate route and introduction of nickel leading to more surface defects. Previous studies have convinced that surface chemisorbed oxygen were more active to oxidize NO than lattice oxygen. And the higher ratio of surface chemisorbed oxygen facilitate the “fast-SCR” reaction.<sup>10</sup>

The Mn2p spectra were deconvoluted into three peaks located at 641.0, 642.4 and 643.8 eV, which can be assigned to  $Mn^{2+}$ ,  $Mn^{3+}$  and  $Mn^{4+}$ , respectively.<sup>30,31</sup> The percentage of Mn species with different valences was calculated, and the results were shown in Table 2. Although a higher oxidation state of manganese species was better for redox properties,<sup>32</sup> moderate

ratio of  $Mn^{3+}/Mn^{4+}$  was help to improve  $SO_2 + H_2O$  resistance. In our study, the surface  $Mn^{3+}$  species was related to  $SO_2 + H_2O$  resistance. As shown in Table 2, the sequence of  $Mn^{3+}$  species was 6Mn4Ce-O > 6Mn4Ce-N > 6Mn4Ce-C, consistent with catalytic sequence in Fig. 1B. For samples from oxalate route, the sequence of  $Mn^{3+}$  species was 1Ni6Mn3Ce-O > 6Mn4Ce-O > 1Co6Mn3Ce-O, indicating a third dopant can regulate the surface manganese species. Based on the above various characterization studies, it was observed that different preparation method or a third dopant can regulate interaction among Mn, Ce, Ni/Co oxides, which would bring about an appropriate content of active  $Mn^{3+}$  and oxygen species on the surface of catalyst.

**3.2.3 Temperature programming.** Redox properties are crucial for the  $NH_3$ -SCR activities, and  $H_2$ -TPR spectra were employed to investigate redox properties of the catalysts. The  $H_2$  consumption as a function of reaction temperature was shown in Fig. 5. For 6Mn4Ce-O, three reduction peaks were observed. The peak centered at  $286$  °C could be assigned to reduction of  $Mn^{4+} \rightarrow Mn^{3+}$ , and the peak centered at  $243$  °C could be ascribed to  $Mn^{3+} \rightarrow Mn^{2+}$ . The broad peak at  $381$  °C was related to the reduction of surface oxygen of  $CeO_2$  ( $Ce^{4+} \rightarrow Ce^{3+}$ ).<sup>33</sup> There was no significant peaks related to  $Mn^{3+} \rightarrow Mn^{2+}$  for samples prepared from nano-casting route and co-precipitation route, consistent with XPS and XRD results, indicating their less portion of  $Mn^{3+}$ . While for 1Ni6Mn3Ce-O and 1Co6Mn3Ce-O, all peaks shifted to lower temperature range, indicating the incorporation of Ni/Co, Mn and Ce enhances the reducibility of catalyst.

$NH_3$ -TPD was employed to investigate  $NH_3$  adsorption, therefore to examine the acidic sites on different catalysts, as presented in Fig. 6. There were two main peaks on all spectra. The peak at the mid-temperature range (100–400 °C) is related to the desorption of  $NH_3$  coordinated to Lewis acid sites, and the peak at high-temperature range (400–550 °C) is considered to the desorption of  $NH_3$  coordinated to Brønsted acid sites.<sup>15,34</sup> Compared with catalysts prepared from nano-casting and precipitation method, the peak related to Lewis acid sites of

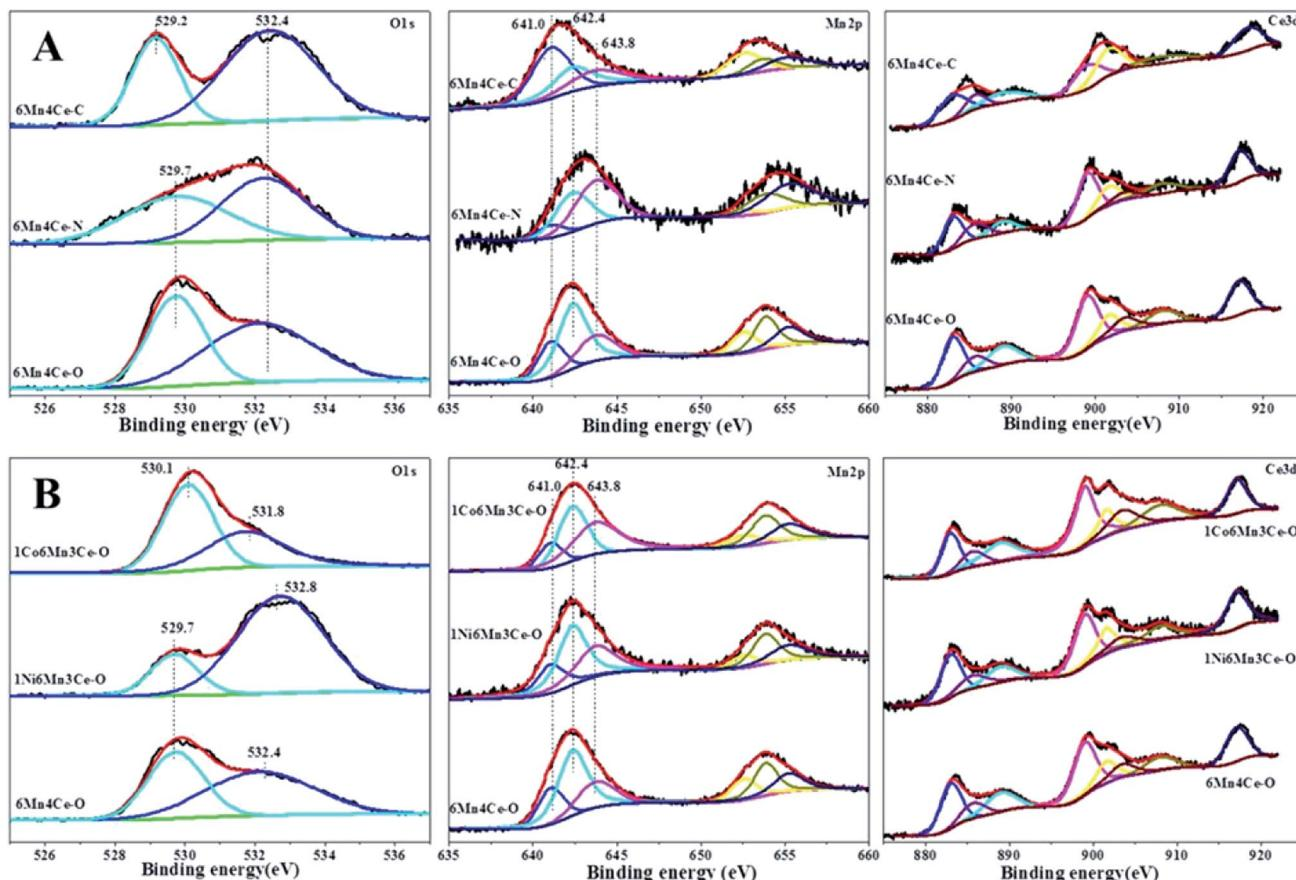


Fig. 4 O1s, Mn2p and Ce3d spectra of (A) samples from different methods, and (B) nickel or cobalt doped samples from oxalate route.

Table 2 The relative ratio of different elements for all catalysts

O <sub>ads</sub> /O <sub>latt</sub>	Mn <sup>2+</sup> (%)	Mn <sup>3+</sup> (%)	Mn <sup>4+</sup> (%)	B/L	
6Mn4Ce-O	1.96	21.89	55.34	22.77	0.47
6Mn4Ce-N	1.26	9.17	39.08	51.75	0.37
6Mn4Ce-C	1.09	47.31	30.17	22.52	0.29
1Ni5Mn4Ce-O	3.91	20.64	46.73	32.63	0.95
1Co5Mn4Ce-O	0.71	14.56	39.98	45.46	0.39

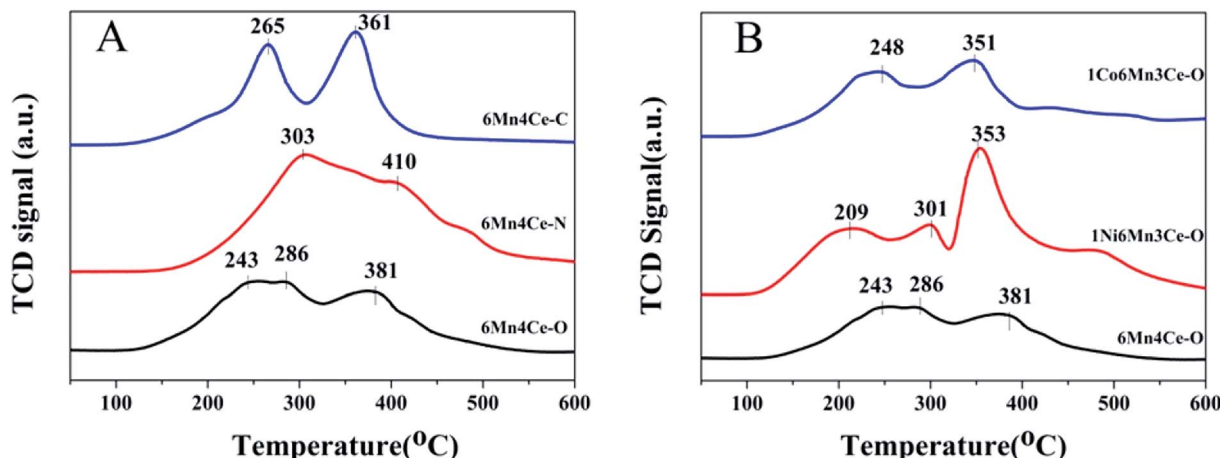
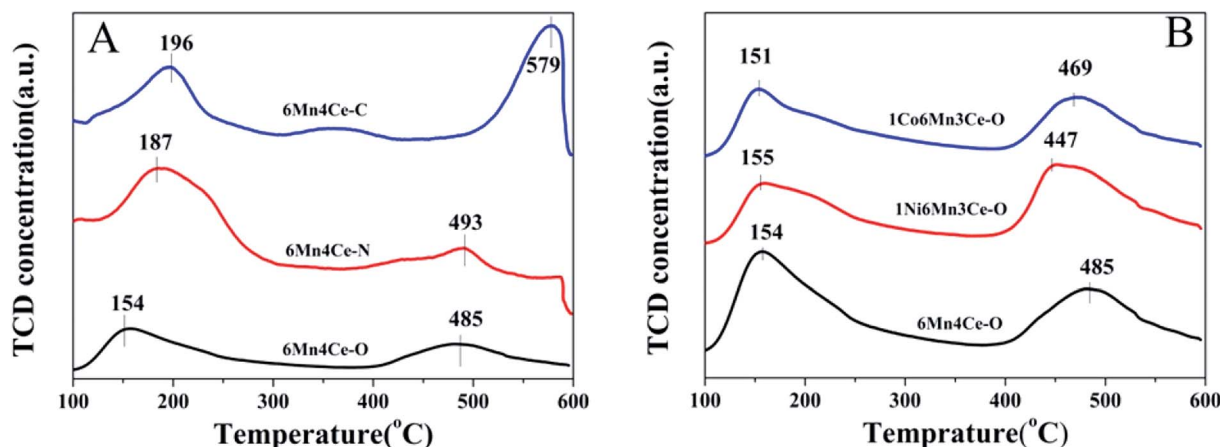
6Mn4Ce-O moved toward lower temperature range, indicating the existence of weak Lewis adsorption sites. As described above, samples from oxalate route may have more acidic sites during the decomposition of precursors. The ratios of NH<sub>3</sub> adsorption on Brønsted acid site to Lewis acid sites of different catalysts are shown in Table 2. Oxalate route was easier to produce more Brønsted acid sites than other two methods. And addition of nickel can greatly increase the ratio of Brønsted acid/Lewis acid sites. Based on the above various characterization studies, it was observed that different preparation method or a third dopant could regulate interaction among Mn, Ce, Ni/Co oxides, which would bring about an appropriate content of active Mn<sup>3+</sup> and oxygen species on the surface of catalyst.

As samples from the oxalate route had different resistance to SO<sub>2</sub> and H<sub>2</sub>O, SO<sub>2</sub>-TPD tests were performed on these three

samples, and the results were shown in Fig. 7. There were two main desorption peaks in the temperature range of 300–600 °C, and 650–800 °C, labeled as 1 and 2, respectively. The small and broad peak in area 1 was reported to be assigned to desorption of SO<sub>2</sub> adsorbed on the surface of catalysts.<sup>35</sup> In this paper, the area labeled 1 of 1Ni5Mn4Ce was slightly smaller than the other two catalysts, which indicated less SO<sub>2</sub> adsorption on it. The main peak at 650–580 °C was associated to desorption of SO<sub>2</sub> released from the decomposition of metal sulfates. The area 2 of 1Ni5Mn4Ce was much smaller compared with others, which indicated nickel adding can inhibit formation of metal sulfates. Similar conclusion could be achieved from the TG-DTA test of samples after SO<sub>2</sub> + H<sub>2</sub>O resistance experiments, as shown in ESI.†

### 3.3 In situ DRIFTS

To better understand gas adsorption on different catalysts from oxalate route, *in situ* DRIFTS was conducted, and the results were shown in Fig. 8. Fig. 8A showed *in situ* DRIFTS spectra of NH<sub>3</sub> + O<sub>2</sub> adsorbed on three samples. The bands at 1235, 1565, 1610 cm<sup>-1</sup> were ascribed to NH<sub>3</sub> coordinated on Lewis acid sites.<sup>36</sup> The band at 1457 cm<sup>-1</sup> was due to the symmetric bending vibration of NH<sub>4</sub><sup>+</sup> chemisorbed on the Brønsted acid sites.<sup>18</sup> Meanwhile, a band at 3230 cm<sup>-1</sup> was due to the N–H stretching vibrations of the NH<sub>4</sub><sup>+</sup>.<sup>37</sup> Comparing with 1Co6Mn3Ce-O, 6Mn4Ce-O and 1Ni6Mn3Ce-O revealed more

Fig. 5  $\text{H}_2$ -TPR spectra of (A) samples from different methods, and (B) nickel or cobalt doped samples from oxalate route.Fig. 6  $\text{NH}_3$ -TPD spectra of (A) samples from different methods, and (B) nickel or cobalt doped samples from oxalate route.

Brønsted acid sites, consistent with  $\text{NH}_3$ -TPD results. Wu obtained the same result that addition of nickel could significantly improve the Brønsted acid sites on  $\text{FeVO}_4/\text{TiO}_2$ .<sup>38</sup>

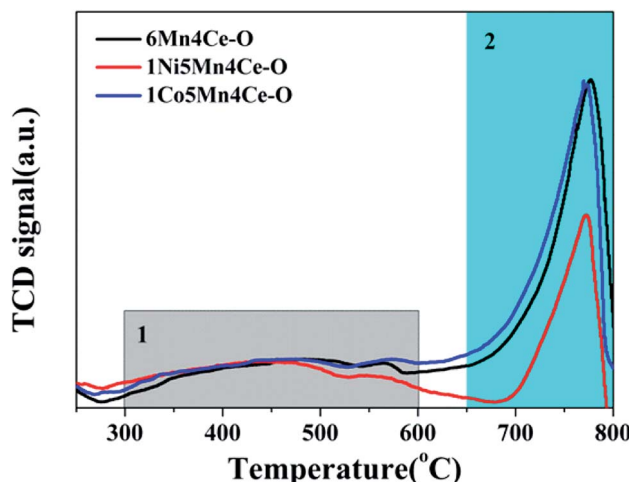
Fig. 7  $\text{SO}_2$ -TPD spectra samples from an oxalate route.

Fig. 8B displayed the *in situ* DRIFTS spectra of  $\text{NO}_x + \text{O}_2$  adsorption on catalysts at 200 °C. The peaks centered at 1606  $\text{cm}^{-1}$  can be ascribed to bridging monodentate nitrates, and peaks centered at 1267, 1209, 1568 and 1540  $\text{cm}^{-1}$  were assigned to bidentate nitrates.<sup>39</sup> It was noteworthy that bidentate nitrates species on 1Ni6Mn3Ce-O were more than those on other catalysts, indicating nickel addition increased NO uptake. However, cobalt doping led to the decrease of bands related to bidentate nitrates, indicating its suppression to NO adsorption.

As 1Ni6Mn3Ce-O showed the best  $\text{H}_2\text{O}$  and  $\text{SO}_2$  resistance, the *in situ* DRIFTS were further displayed to understand the mechanism, and the results were shown in Fig. 9. The 1Ni6Mn3Ce-O was firstly exposed to  $\text{NH}_3$  for 60 min, and then  $\text{SO}_2$  and  $\text{H}_2\text{O}$  was introduced to the reaction gas. The bands corresponding to  $\text{NH}_3(a)$  was quickly diminished, and new bands related to  $\text{SO}_2$  adsorption appeared, as shown in Fig. 9A. While 1Ni6Mn3Ce-O was firstly exposed to  $\text{NO} + \text{O}_2$  for 60 min, and then  $\text{SO}_2$  was introduced to the reaction gas, no new bands appeared, which indicated that NO was more easily adsorbed on the surface of catalysts. The 1Ni6Mn3Ce-O was exposed to  $\text{NH}_3 + \text{NO} + \text{O}_2$  at 200 °C for 60 min, and there were peaks related to

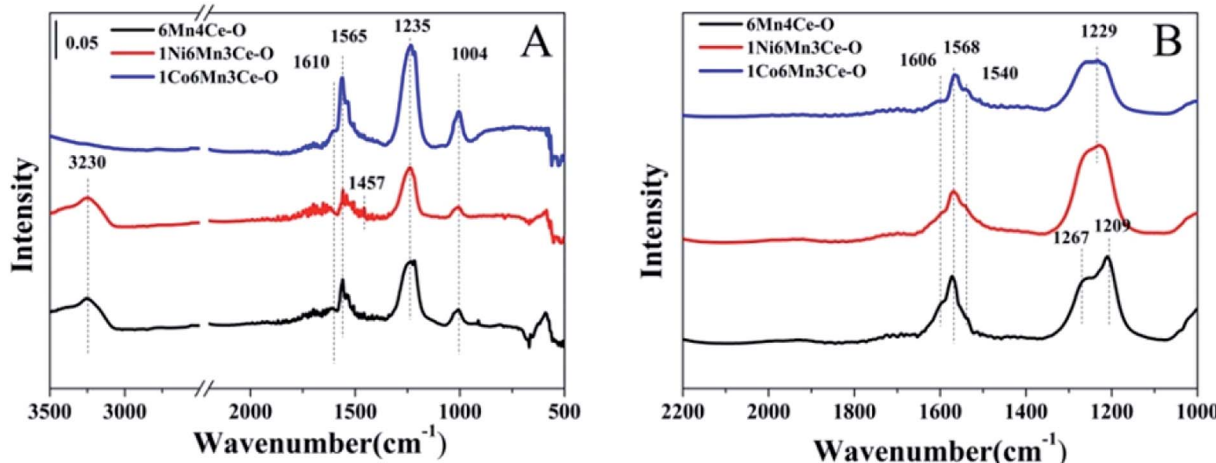


Fig. 8 *In situ* DRIFTS of samples under  $\text{NH}_3 + \text{air}$  (A) and  $\text{NOx} + \text{air}$  (B) for 1 h and then purged by helium for 30 min at  $200^\circ\text{C}$ .

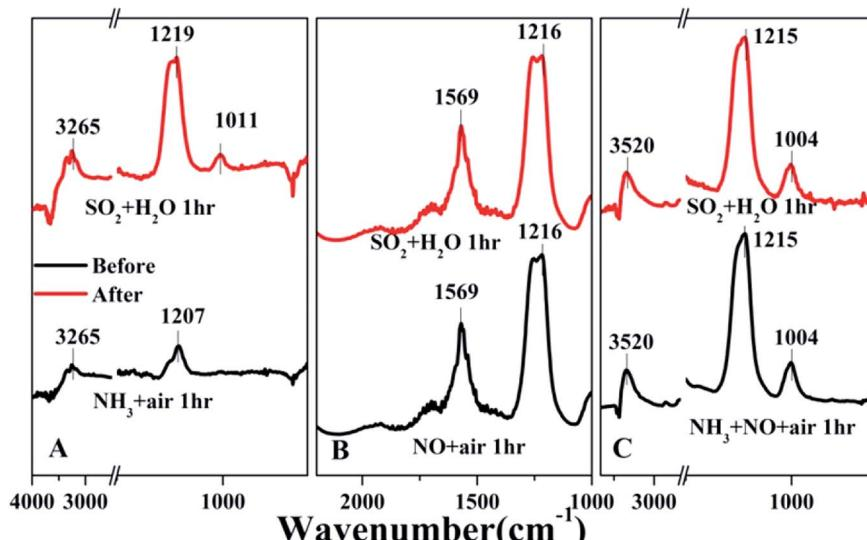


Fig. 9 *In situ* DRIFTS of  $1\text{Ni}6\text{Mn}3\text{Ce-O}$  under  $\text{NH}_3 + \text{air}$  (A),  $\text{NOx} + \text{air}$  (B) and  $\text{NOx} + \text{NH}_3 + \text{O}_2$  (C) for 1 h and then  $\text{SO}_2$  and  $\text{H}_2\text{O}$  were introduced into the mixed gas for 1 h at  $200^\circ\text{C}$ .

$\text{NH}_3$  and  $\text{NOx}$  adsorption, indicating the co-adsorption of  $\text{NH}_3$  and  $\text{NOx}$ . After 100 ppm  $\text{SO}_2$  and  $\text{H}_2\text{O}$  were added for another 60 min, no new bands appeared and the intensity of the original bands remained unchanged. This indicated that  $\text{SO}_2$  and  $\text{H}_2\text{O}$  in the flue gas had no impact on  $\text{NH}_3$ -SCR of  $1\text{Ni}6\text{Mn}3\text{Ce-O}$ , which was in agreement with the results in Fig. 1. The  $\text{NH}_3$ -SCR reaction on  $1\text{Ni}6\text{Mn}3\text{Ce-O}$  may follow L-H mechanism,  $\text{NH}_3(\text{a})$  and  $\text{NO}(\text{a})$  reacted to form  $\text{N}_2$  and  $\text{H}_2\text{O}$ . When  $\text{SO}_2$  and  $\text{H}_2\text{O}$  were introduced into the flue gas,  $\text{NO}(\text{a})$  was more prone to react with  $\text{NH}_3(\text{a})$  than  $\text{SO}_2$ . All of these contribute to excellent  $\text{H}_2\text{O}$  and  $\text{SO}_2$  resistance.

## 4 Discussion and conclusions

It was commonly accepted that there was an intense correlation between catalytic performance and structural properties, such

as morphologies, crystal plans, crystal phases and porous structures. A porous structure provided much surface area and makes the adsorption and diffusion of reactant molecules easy to conduct on the surface of catalysts. In this report, catalysts with different pore structures were created by oxalate route, nanocasting strategy and co-precipitation method. Based on above analysis, catalyst from oxalate route showed best  $\text{NOx}$  conversion, including  $\text{NOx}$  conversion and  $\text{SO}_2$  and  $\text{H}_2\text{O}$  resistance. Catalyst from oxalate route presented proper ratio of  $\text{Mn}^{3+}$ , surface oxygen species, surface acidic sites, moderate pore size and specific surface area.

Because the catalytic process over single oxide catalysts was limited, the addition of another component into the system would be favorable.<sup>28</sup> In this study, cobalt or nickel was added to Mn-Ce composites, which enhanced the interaction between different elements. However, the de $\text{NOx}$  performances of

catalysts were varied based on the added elements. The introduction of nickel leads to the co-existence of Lewis acid sites and Brønsted acid sites. Addition of cobalt leads to much more Lewis acid sites. It has been proved in previous analysis that Brønsted acid sites are better for the resistance of  $H_2O$  and  $SO_2$ .

Several methods have been developed to reduce the poisonous effect of  $H_2O$  and  $SO_2$  to SCR, such as selecting most active support, metal modification, rational design of structure and morphology,<sup>41</sup> and pre-sulfation.<sup>40,41</sup> The mechanism of these methods was to make a balance among redox properties, effective acid sites, and the formation/decomposition of ammonium sulfate, therefore enhancing the deNOx properties and suppressing the blocking effect of  $H_2O$  and  $SO_2$ . In this study, introducing nickel into Mn–Ce composite gave rise to more Brønsted acid sites, which was responsible for good  $H_2O$  and  $SO_2$  resistance.

Different preparation method including oxalate route, nanocasting strategy and traditional co-precipitation were applied to obtain MnOx–CeO<sub>2</sub> mixed oxides. The mesoporous Mn–Ce base catalysts prepared from oxalate route showed high deNOx efficiency and good  $SO_2$  and  $H_2O$  resistance in the low temperature range. A third dopant such as nickel or cobalt was introduced to the composite to increase  $SO_2$  and  $H_2O$  durability. The nickel–manganese–cerium ternary oxides showed the best  $SO_2$  and  $H_2O$  durability. The reason can be ascribed to its smaller pores and amorphous structure and proper amount of surface Mn<sup>3+</sup>/oxygen species, which could decrease the chemical adsorption of  $SO_2$ .

## Conflicts of interest

There are no conflicts to declare.

## Acknowledgements

The research was financially supported by the National Key Research and Development Plan (2016YFC0204100, 2016YFC0204103), Control Strategy and Technology Integrated Demonstration of Industrial Source Pollution in Guanzhong area of China (ZDRW-ZS-2017-6-2). The authors also acknowledge the analytical and testing center of Institute of Process Engineering, Chinese Academy of Sciences, for their extensive help in testing of samples.

## References

- 1 C. Gao, J. W. Shi, Z. Y. Fan, G. Gao and C. M. Niu, Sulfur and Water Resistance of Mn-Based Catalysts for Low-Temperature Selective Catalytic Reduction of NOx: a Review, *Catalysts*, 2018, **8**, 11.
- 2 L. Q. Chen, F. L. Yuan, Z. B. Li, X. Y. Niu and Y. J. Zhu, Synergistic effect between the redox property and acidity on enhancing the low temperature NH<sub>3</sub>-SCR activity for NOx removal over the Co<sub>0.2</sub>Ce<sub>x</sub>Mn<sub>0.8-x</sub>Ti<sub>10</sub> (x=0-0.40) oxides catalysts, *Chem. Eng. J.*, 2018, **354**, 393–406.
- 3 X. Hu, L. Huang, J. Zhang, H. Li, K. Zha, L. Shi, *et al.*, Facile and template-free fabrication of mesoporous 3D nanosphere-like Mn<sub>x</sub>Co<sub>3-x</sub>O<sub>4</sub> as highly effective catalysts for low temperature SCR of NOx with NH<sub>3</sub>, *J. Mater. Chem. A*, 2018, **6**, 2952–2963.
- 4 L. Li, B. Sun, J. Sun, S. Yu, C. Ge, C. Tang, *et al.*, Novel MnOx–CeO<sub>2</sub> nanosphere catalyst for low-temperature NH<sub>3</sub>-SCR, *Catal. Commun.*, 2017, **100**, 98–102.
- 5 C. Li, X. Tang, H. Yi, L. Wang, X. Cui, C. Chu, *et al.*, Rational design of template-free MnOx–CeO<sub>2</sub> hollow nanotube as de-NOx catalyst at low temperature, *Appl. Surf. Sci.*, 2018, **428**, 924–932.
- 6 H. Chang, J. Li, X. Chen, L. Ma, S. Yang, J. W. Schwank, *et al.*, Effect of Sn on MnOx–CeO<sub>2</sub> catalyst for SCR of NOx by ammonia: Enhancement of activity and remarkable resistance to  $SO_2$ , *Catal. Commun.*, 2012, **27**, 54–57.
- 7 J. Liu, R.-t Guo, M.-y Li, P. Sun, S.-m. Liu, W.-g. Pan, *et al.*, Enhancement of the  $SO_2$  resistance of Mn/TiO<sub>2</sub> SCR catalyst by Eu modification: A mechanism study, *Fuel*, 2018, **223**, 385–393.
- 8 Z. Liu, X. Feng, Z. Zhou, Y. Feng and J. Li, Ce–Sn binary oxide catalyst for the selective catalytic reduction of NOx by NH<sub>3</sub>, *Appl. Surf. Sci.*, 2018, **428**, 526–533.
- 9 K. Zha, S. Cai, H. Hu, H. Li, T. Yan, L. Shi, *et al.*, In Situ DRIFTS Investigation of Promotional Effects of Tungsten on MnOx–CeO<sub>2</sub>/meso-TiO<sub>2</sub> Catalysts for NOx Reduction, *J. Phys. Chem. C*, 2017, **121**, 25243–25254.
- 10 F. Gao, X. Tang, H. Yi, J. Li, S. Zhao, J. Wang, *et al.*, Promotional mechanisms of activity and  $SO_2$  tolerance of Co- or Ni-doped MnOx–CeO<sub>2</sub> catalysts for SCR of NOx with NH<sub>3</sub> at low temperature, *Chem. Eng. J.*, 2017, **317**, 20–31.
- 11 K. Zha, L. Kang, C. Feng, L. Han, H. Li, T. Yan, *et al.*, Improved NOx reduction in the presence of alkali metals by using hollandite Mn–Ti oxide promoted Cu-SAPO-34 catalysts, *Environ. Sci. Nano*, 2018, **5**, 1408–1419.
- 12 L. Kang, L. Han, J. He, H. Li, T. Yan, G. Chen, *et al.*, Improved NOx Reduction in the Presence of  $SO_2$  by Using Fe<sub>2</sub>O<sub>3</sub>-Promoted Halloysite-Supported CeO<sub>2</sub>–WO<sub>3</sub> Catalysts, *Environ. Sci. Technol.*, 2019, **53**, 938–945.
- 13 F. Kleitz, S. Hei Choi and R. Ryoo, Cubic Ia3d large mesoporous silica: synthesis and replication to platinum nanowires, carbon nanorods and carbon nanotubes, *Chem. Commun.*, 2003, 2136–2137.
- 14 H. Liu, L. Wei, R. Yue and Y. Chen, CrOx–CeO<sub>2</sub> binary oxide as a superior catalyst for NO reduction with NH<sub>3</sub> at low temperature in presence of CO, *Catal. Commun.*, 2010, **11**, 829–833.
- 15 J. Liu, X. Li, R. Li, Q. Zhao, J. Ke, H. Xiao, *et al.*, Facile synthesis of tube-shaped Mn–Ni–Ti solid solution and preferable Langmuir–Hinshelwood mechanism for selective catalytic reduction of NOx by NH<sub>3</sub>, *Appl. Catal., A*, 2018, **549**, 289–301.
- 16 Y. Wan, W. Zhao, Y. Tang, L. Li, H. Wang, Y. Cui, *et al.*, Ni–Mn bi-metal oxide catalysts for the low temperature SCR removal of NO with NH<sub>3</sub>, *Appl. Catal., B*, 2014, **148–149**, 114–122.
- 17 X. Li, Y. Du, X. Guo, R. Wang, B. Hou and X. Wu, Synthesis of a Novel NiMnTi Mixed Metal Oxides from LDH Precursor



and Its Catalytic Application for Selective Catalytic Reduction of NOx with NH<sub>3</sub>, *Catal. Lett.*, 2018, **149**, 456–464.

18 H. Chang, X. Chen, J. Li, L. Ma, C. Wang, C. Liu, *et al.*, Improvement of Activity and SO<sub>2</sub> Tolerance of Sn-Modified MnO<sub>x</sub>-CeO<sub>2</sub> Catalysts for NH<sub>3</sub>-SCR at Low Temperatures, *Environ. Sci. Technol.*, 2013, **47**, 5294–5301.

19 B. Thirupathi and P. G. Smirniotis, Co-doping a metal (Cr, Fe, Co, Ni, Cu, Zn, Ce, and Zr) on Mn/TiO<sub>2</sub> catalyst and its effect on the selective reduction of NO with NH<sub>3</sub> at low-temperatures, *Appl. Catal., B*, 2011, **110**, 195–206.

20 X. Tang, J. Li, L. Wei and J. Hao, MnO<sub>x</sub>-SnO<sub>2</sub> catalysts synthesized by a redox coprecipitation method for selective catalytic reduction of NO by NH<sub>3</sub>, *Chin. J. Catal.*, 2008, **29**, 531–536.

21 S. Li, B. Huang and C. Yu, A CeO<sub>2</sub>-MnO<sub>x</sub> core-shell catalyst for low-temperature NH<sub>3</sub>-SCR of NO, *Catal. Commun.*, 2017, **98**, 47–51.

22 L. Chen, X. Niu, Z. Li, Y. Dong, Z. Zhang, F. Yuan, *et al.*, Promoting catalytic performances of Ni-Mn spinel for NH<sub>3</sub>-SCR by treatment with SO<sub>2</sub> and H<sub>2</sub>O, *Catal. Commun.*, 2016, **85**, 48–51.

23 W. Sun, X. Li, Q. Zhao, M. Tade and S. Liu, W<sub>x</sub>Mn<sub>1-x</sub>O<sub>x</sub> Catalysts Synthesized by a One-Step Urea Co-precipitation Method for Selective Catalytic Reduction of NOx with NH<sub>3</sub> at Low Temperatures, *Energy Fuels*, 2016, **30**, 1810–1814.

24 N. Fang, J. Guo, S. Shu, H. Luo, Y. Chu and J. Li, Enhancement of low-temperature activity and sulfur resistance of Fe<sub>0.3</sub>Mn<sub>0.5</sub>Zr<sub>0.2</sub> catalyst for NO removal by NH<sub>3</sub>-SCR, *Chem. Eng. J.*, 2017, **325**, 114–123.

25 G. Qi and R. T. Yang, Performance and kinetics study for low-temperature SCR of NO with NH<sub>3</sub> over MnO<sub>x</sub>-CeO<sub>2</sub> catalyst, *J. Catal.*, 2003, **217**, 434–441.

26 M. Qiu, S. Zhan, H. Yu and D. Zhu, Low-temperature selective catalytic reduction of NO with NH<sub>3</sub> over ordered mesoporous Mn<sub>x</sub>Co<sub>3-x</sub>O<sub>4</sub> catalyst, *Catal. Commun.*, 2015, **62**, 107–111.

27 P. Zhang, Y. Sun, W. Su, Y. Wei and J. Liu, Low-temperature selective catalytic reduction of NO with NH<sub>3</sub> over Ni-Mn-Ox catalysts, *RSC Adv.*, 2016, **6**, 107270–107277.

28 W. Tang, Y. Deng, W. Li, J. Li, G. Liu, S. Li, *et al.*, Importance of porous structure and synergistic effect on the catalytic oxidation activities over hierarchical Mn-Ni composite oxides, *Catal. Sci. Technol.*, 2016, **6**, 1710–1718.

29 B. Jia, J. Guo, H. Luo, S. Shu, N. Fang and J. Li, Study of NO removal and resistance to SO<sub>2</sub> and H<sub>2</sub>O of MnO<sub>x</sub>/TiO<sub>2</sub>, MnO<sub>x</sub>/ZrO<sub>2</sub> and MnO<sub>x</sub>/ZrO<sub>2</sub>-TiO<sub>2</sub>, *Appl. Catal., A*, 2018, **553**, 82–90.

30 Q. Shen, L. Zhang, N. Sun, H. Wang, L. Zhong, C. He, *et al.*, Hollow MnO<sub>x</sub>-CeO<sub>2</sub> mixed oxides as highly efficient catalysts in NO oxidation, *Chem. Eng. J.*, 2017, **322**, 46–55.

31 W. Sun, X. Li, Q. Zhao, J. Mu and J. Chen, Fe-Mn Mixed Oxide Catalysts Synthesized by One-Step Urea-Precipitation Method for the Selective Catalytic Reduction of NOx with NH<sub>3</sub> at Low Temperatures, *Catal. Lett.*, 2018, **148**, 227–234.

32 D. S. Zhang, L. Zhang, L. Y. Shi, C. Fang, H. R. Li, R. H. Gao, *et al.*, In situ supported MnO<sub>x</sub>-CeO<sub>x</sub> on carbon nanotubes for the low-temperature selective catalytic reduction of NO with NH<sub>3</sub>, *Nanoscale*, 2013, **5**, 1127–1136.

33 Y. Niu, T. Shang, S. Hui, X. Zhang, Y. Lei, Y. Lv, *et al.*, Synergistic removal of NO and N<sub>2</sub>O in low-temperature SCR process with MnO<sub>x</sub>/Ti based catalyst doped with Ce and V, *Fuel*, 2016, **185**, 316–322.

34 J. Liu, X. Li, Q. Zhao, J. Ke, H. Xiao, X. Lv, *et al.*, Mechanistic investigation of the enhanced NH<sub>3</sub>-SCR on cobalt-decorated Ce-Ti mixed oxide: In situ FTIR analysis for structure-activity correlation, *Appl. Catal., B*, 2017, **200**, 297–308.

35 L. Chen, R. Li, Z. Li, F. Yuan, X. Niu and Y. Zhu, Effect of Ni doping in Ni<sub>x</sub>Mn<sub>1-x</sub>Ti<sub>10</sub> (x = 0.1–0.5) on activity and SO<sub>2</sub> resistance for NH<sub>3</sub>-SCR of NO studied with in situ DRIFTS, *Catal. Sci. Technol.*, 2017, **7**, 3243–3257.

36 H.-D. Liu, W.-M. Li, R.-L. Yue and Y.-F. Chen, Reaction Mechanism of NH<sub>3</sub>-Selective Catalytic Reduction for NO on CrO<sub>x</sub>-CeO<sub>2</sub> Binary Oxide, *Chin. J. Inorg. Chem.*, 2013, **29**, 2399–2404.

37 T. Zhang, F. Qiu, H. Chang, Y. Peng and J. Li, Novel W-modified SnMnCeO<sub>x</sub> catalyst for the selective catalytic reduction of NOx with NH<sub>3</sub>, *Catal. Commun.*, 2017, **100**, 117–120.

38 G. Wu, X. Feng, H. Zhang, Y. Zhang, J. Wang, Y. Chen, *et al.*, The promotional role of Ni in FeVO<sub>4</sub>/TiO<sub>2</sub> monolith catalyst for selective catalytic reduction of NOx with NH<sub>3</sub>, *Appl. Surf. Sci.*, 2018, **427**, 24–36.

39 W. Shan, F. Liu, H. He, X. Shi and C. Zhang, Novel cerium-tungsten mixed oxide catalyst for the selective catalytic reduction of NOx with NH<sub>3</sub>, *Chem. Commun.*, 2011, **47**, 8046–8048.

40 K. Wijayanti, S. Andonova, A. Kumar, J. Li, K. Kamasamudram, N. W. Currier, *et al.*, Impact of sulfur oxide on NH<sub>3</sub>-SCR over Cu-SAPO-34, *Appl. Catal., B*, 2015, **166**, 568–579.

41 L. Zhang, H. Qu, T. Du, W. Ma and Q. Zhong, H<sub>2</sub>O and SO<sub>2</sub> tolerance, activity and reaction mechanism of sulfated Ni-Ce-La composite oxide nanocrystals in NH<sub>3</sub>-SCR, *Chem. Eng. J.*, 2016, **296**, 122–131.

